ROYAL SOCIETY
OF CHEMISTRY

PAPER

Check for updates

Dynamic magnetic properties and spin pumping in polymer-assisted-deposited La$_{0.92}$MnO$_3$ thin films

Hailin Wang, [ID] Alberto Pomar, [ID]* Sergi Martín-Rio, [ID] Carlos Frontera, [ID] Narcis Mestres [ID] and Benjamín Martínez [ID]

Complex oxide thin films grown by using chemical methods are of strong interest because of their low-cost, environment friendly fabrication and easy scalability. However, their introduction in spintronic applications or magnetic devices is still scarce mainly because of concerns regarding their interfacial quality. Here, we report on the preparation by polymer-assisted-deposition (PAD) of epitaxial La$_{0.92}$MnO$_3$ (LMO) thin films. We demonstrate that ferromagnetic conducting LMO thin films with smooth surfaces (rms ∼ 0.2 nm) can be prepared by PAD. By means of temperature-dependent broadband ferromagnetic resonance (FMR), we show that the LMO film exhibits a four-fold in-plane anisotropy, with [110] being the easy in-plane axis, compatible with strain release from the rhombohedral bulk phase. It has also been found that the isotropic Gilbert damping, α, determined from the broadening of the FMR linewidth, does not show a relevant extrinsic contribution and it exhibits an intraband-like temperature dependence, *i.e.* it increases as temperature decreases. By capping LMO thin films with a 10 nm thick Pt layer deposited *ex situ*, damping is substantially enhanced, from a value at 150 K of $\alpha_{LMO} \sim 1 \times 10^{-2}$ for the bare LMO film to $\alpha_{LMO+Pt} \sim 2.5 \times 10^{-2}$ for the Pt capped film. This strong increase of magnetic damping is indicative of the transfer of spin momentum from LMO to the Pt layer by spin pumping. Our results demostrate that LMO films grown by PAD may be used as efficient spin source systems in heterostructures for spintronic devices.

1 Introduction

The utilization of transition metal oxides in spintronic applications relies on the availability of high-quality thin films that may be helpful in the ever-increasing demands of miniaturization and reduced power consumption. Among the different promising technologies, devices based on the spin transfer torque effect are very appealing due to the possibility of manipulating spin configurations in an efficient way with low power consumption.[1] Thus, a noticeable effort has been devoted to studying the magnetization switching processes, crucial to spin torque phenomena and, in particular, to understanding and controling magnetic damping.[2,3] In general, low magnetic damping constants may be achieved in transition metal oxide films, either in insulating materials as yttrium iron garnet[4] or in half-metallic compounds as La$_{2/3}$Sr$_{1/3}$MnO$_3$.[5] In the last case, the main drawback arises from the important extrinsic contribution to damping associated with the scattering of conduction electrons by the two magnon mechanism.[6] This extrinsic damping is enhanced by the presence of surface/interface roughness or magnetic inhomogenity originating from the defect landscape of the film. Nevertheless, a tough tuning of the growth conditions

allows obtaining intrinsic damping values in the order of 10^{-3} for films grown by using physical methods (pulsed laser deposition, sputtering or molecular beam epitaxy).[2] These low Gilbert damping values open the possibility to use half-metallic manganite-based oxides to generate pure spin currents by, for example, spin pumping into a non magnetic metal. Although few investigations have been made, there are already several promising results proving this approach.[7–10]

The strong activity in the field has boosted a fast improvement in the quality of grown thin films. Although high-vacuum methods, such as molecular beam epitaxy,[11] RF sputtering[12] and pulsed laser deposition,[13–15] offer unquestionable advantages for the growth of metal oxide thin films like high crystal quality, precise control of composition and thickness at atomic-scale even for several unit cell thick films, more affordable alternatives are desirable. Generally speaking, chemical deposition techniques offer the ability to grow over large areas at low cost and the versatility to easily tune stoichiometry in complex oxides makes chemical deposition techniques very appealing. In particular, polymer assisted deposition (PAD) has appeared as a competitive route for environment friendly approaches as it is based on the deposition of cationic aqueous solutions.[16] It is also worth noting that since the aqueous PAD precursor solutions are largely stable, they enable setting a metal library easily to be mixed afterwards to obtain finely compositionally controlled complex oxides.

Instituto de Ciencia de Materiales de Barcelona, ICMAB-CSIC, Campus de la UAB, 08193 Bellaterra, Spain. E-mail: apomar@icmab.es; Tel: +34 935801853

This journal is © The Royal Society of Chemistry 2019

J. Mater. Chem. C, 2019, **7**, 12633–12640 | **12633**

Moreover, although larger processing times may appear as a drawback, the slow growth conditions of PAD close to thermodynamic equilibrium conditions are adequate for the epitaxial growth of ternary and complex oxides as has already been demonstrated for a large variety of oxide films.[17,18] Since the energy balance involved during the growth process is quite delicate, chemical growth methods may lead to a defect landscape different from that generated by using vacuum techniques, resulting in the modification of the physical properties of the films, as for example, magnetic anisotropy.[19] In spite of their importance, the dynamic magnetic properties of chemically grown films remain an open and unexplored topic.

The main aim of this work is to study the magnetic anisotropy and damping of oxide thin films grown by PAD and to demonstrate that they are suitable for spintronic applications. For this, we have selected the ferromagnetic-metallic $La_{0.92}MnO_3$. $LaMnO_3$, the parent compound of the colossal magnetoresistance family of manganite perovskites, has recently regained new attention as an oxide catalyst for fuel cells and metal–air batteries,[20] and as an electrode material for supercapacitors,[21] as well as due to its unexpected ferromagnetic behavior in thin films.[22–24] Although bulk stoichiometric $LaMnO_3$ is a Mott insulator and an A-type antiferromagnet (AF), in thin film form, its properties may be tuned into a ferromagnetic (FM) state due to the structural strain induced by the substrate[25,26] or by introducing ion vacancies (both in La and Mn sites) in the material.[27–29] However, $LaMnO_3$ is a complex system where it is very difficult to disentangle the effects of strain, oxygenation and cation vacancies on the magnetic state. On one hand, theoretical studies indicated that the FM behavior in $LaMnO_3$ thin films originates from the strain-induced orbital ordering[26] and this mechanism was invoked to explain the tuning between AF and FM states in stoichiometric $LaMnO_3$ thin films prepared under different growth oxygen pressures.[25] On the other hand, the dependence of magnetic properties on film thickness is still puzzling as, while an increase of saturation magnetization and transition temperature with increasing thickness was reported for films grown on $SrTiO_3$,[30] the opposite seems to occur for films grown on $LaAlO_3$ substrates.[31] It is worth noting that, in the case of stoichiometric samples, the material exhibits an insulating character in both the AF and the FM states.[25] However, in the presence of cationic vacancies, to preserve charge neutrality, a mixed Mn^{3+} and Mn^{4+} valence state appears. This mixed valence state promotes the appearance of double exchange interaction *via* oxygen atoms driving the system into a ferromagnetic and metallic state.[28] As an example, 8% of La site vacancies in $LaMnO_3$ creates 24% of holes at the Mn sites leading to a robust ferromagnetic ordering. This is the amount of holes present in $La_{0.76}Ca_{0.24}MnO_3$, for example, although the smaller cationic disorder in $La_{0.92}MnO_3$ makes its electronic conductivity much larger, and its Curie temperature increases up to values close to $T_c = 300$ K making it interesting for spintronic applications. In this work, we have studied, by broadband ferromagnetic resonance, the magnetodynamic properties of ferromagnetic $La_{0.92}MnO_3$ thin films prepared by PAD. The interest of this research is twofold. First, from a materials point of view, it is crucial to investigate if the continuous progress in the quality of PAD films may overcome the challenging difficulties

of roughness and homogeneity control even for properties highly dependent on defect structure as magnetic damping. Second, from a physics point of view, an attempt is made to clarify the mechanisms controlling the magnetodynamic behavior, which will be fundamental for future prospects.

2 Thin film growth and characterization

The $La_{0.92}MnO_3$ (LMO) thin films studied in this work were grown by polymer-assisted-deposition (PAD) on (001)-$SrTiO_3$ (STO) single-crystal substrates. Individual solutions of the different metal ions were prepared by dissolving the corresponding La and Mn nitrates in water with ethylenediaminetetraacetic acid (EDTA, 1:1 molar ratio) and polyethylenimine (PEI), Sigma Aldrich, Ref 408727, with an average molecular weight of 25 000 (1:1 mass ratio to EDTA). Each individual solution was filtrated using Amicon filtration units (10 kDa), and retained portions were analyzed by Inductively Coupled Plasma (ICP) spectroscopy (Optima 4300 DV™ ICP-OES PerkinElmer). The solutions were mixed according to the desired La:Mn 0.92:1 final stoichiometry ratio and spin coated on top of 5 × 5 mm² (001)-$SrTiO_3$ (STO) substrates purchased from Crystec GmbH, Germany. The as-received substrates were chemically etched and thermally treated to make them TiO_2-terminated with atomically flat terraces.[32] After the deposition of the polymeric layer, it was annealed in a horizontal tube furnace under oxygen flow at 950 °C for 30 min. The results discussed in this paper correspond to the layers of LMO of 10 nm as determined by X-ray reflectometry. They were obtained using solutions with a total cation concentration of 139 mM and a rate of 5000 rpm for 90 seconds during spinning.

Systematic θ–2θ X-ray measurements as shown in Fig. 1(a) demonstrate that LMO thin films are in a single phase with no signatures of reflections other than the standard pseudocubic (00*l*) ones. High crystallinity and excellent out-of-plane orientation of the film were evidenced by the low values, less than 0.1°, of the full-width at half-maximum (FWHM) of the rocking curves around the (002) reflection peak (see the inset in Fig. 1(a)). In Fig. 1(b), we show the detail of the θ–2θ scan around the (002) diffraction peak where the deconvolution of the substrate and film peaks is indicated by the corresponding lines. Fitting of the (00*l*) peak positions leads to a pseudocubic out-of-plane parameter of $a_\perp \sim$ 3.87 Å. The strain state of the LMO films was studied by using reciprocal space maps around $(-103)_{STO}$ reflections, as shown in Fig. 1(c). As thin film reflection is very close to the substrate one, in this case, to increase the signal-to-noise ratio, thicker films (~20 nm) were used. The in-plane lattice parameter of the LMO film, $a_\parallel$, matches that of the substrate one, *i.e.*, $a_\parallel = 3.905$ Å. With these $a_\parallel$ and $a_\perp$ values, a rough estimation of pseudocubic volume can be calculated leading to $V_{pc} = a_\parallel^2 a_\perp \sim 59.0$ Å³. The above obtained values may be compared with the reported bulk ones. It is known that the crystal structure of $LaMnO_3$ perovskite strongly depends on oxygen content. In particular, for La-deficient $La_{0.92}MnO_x$ samples, a transition has been reported from the

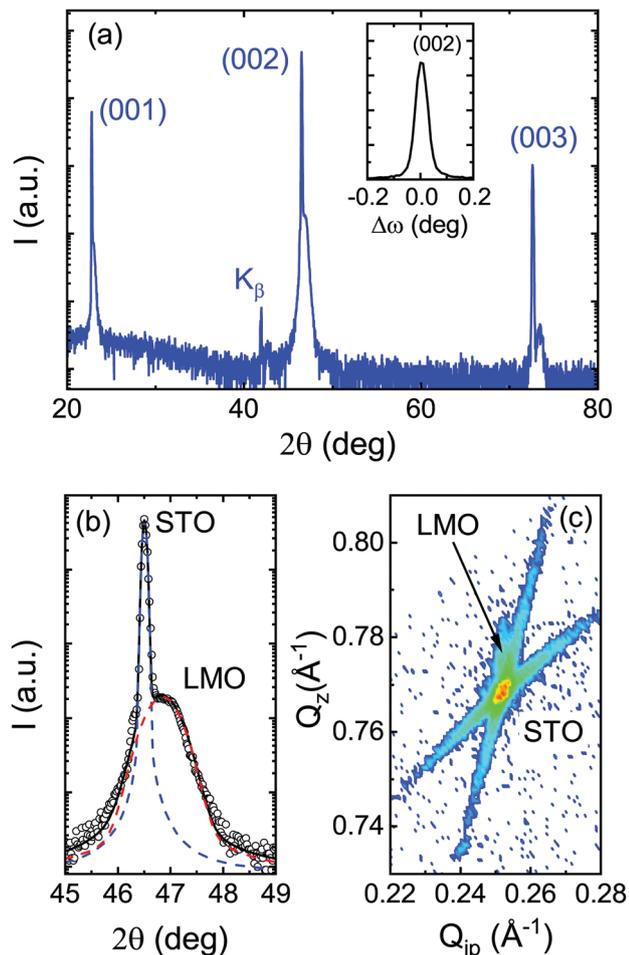12634 | *J. Mater. Chem. C*, 2019, **7**, 12633–12640

This journal is © The Royal Society of Chemistry 2019

Fig. 1 (a) X-ray $\theta-2\theta$ scan of the $La_{0.92}MnO_3$ thin film on a $SrTiO_3$ substrate. For the LMO film, only (00*l*) reflections were observed. The inset shows the rocking curve obtained around the (002) reflection of LMO exhibiting a FWHM = 0.06°. (b) Details of the $\theta-2\theta$ scan around the $(002)_{STO}$ reflection showing the deconvolution between the STO substrate peak (blue lines) and the LMO peak (red lines). (c) Reciprocal space map of the $(-103)_{STO}$ peak revealing in-plane compressive strain in the films. Pseudocubic notation is always used.
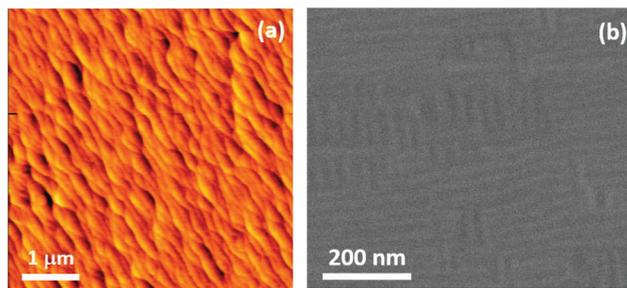

Fig. 2 (a) Topography of the surface of a LMO thin film obtained *via* atomic force microscopy in tapping mode. Terrace-step morphology inherited from the underlying STO substrate can be seen. Overall roughness rms ~ 0.2 nm. (b) Scanning electron microscopy of a LMO thin film. The observation of arrays of alternating dark and clear fringes suggests the formation of ordered rhombohedral twin domains. These two features in (a) and (b) demonstrate the high quality of the surfaces of films prepared by using chemical methods.

orthorhombic *Pnma* structure for *x* = 2.88 to a rhombohedral $R\bar{3}c$ one for *x* = 2.98.[33] Concomitant to this structural evolution, unit cell volume is reduced from $V_{ort} = 61.0$ Å^3 for *Pnma* to $V_{rh} = 58.9$ Å^3 for $R\bar{3}c$. Furthermore, rhombohedral lattice parameters $a_{rh} = 5.477$ Å and $\alpha_{rh} = 60.614°$ correspond to a pseudocubic matching distance of $a_{pc} = 1/2\sqrt{3 - 2\cos\alpha_{rh}} \sim 3.89$ Å leading to a +0.4% tensile mismatch by the STO substrate.[34] Thus, our experimental results suggest a strain accommodation mainly through elastic mechanisms from the rhombohedral phase.[35]

Morphological characteristics of the LMO film surfaces were analyzed *via* Atomic Force Microscopy (AFM) in tapping mode. Under optimal growth conditions, films develop an atomically flat surface that mimics the terrace-step morphology of the surface of the underlying STO substrate, as shown in Fig. 2(a). Quantitative analysis of a 5 μm × 5 μm image indicates a flat surface with rms ~ 0.25 nm, *i.e.*, less than one unit cell. Further confirmation of the high quality of the surface

morphology and microstructure of the films was obtained *via* scanning electron microscopy (SEM). Fig. 2(b) shows a typical SEM image of a 10 nm thick LMO film. In this image, taken at a small tilting angle of 2°, we may observe the occurrence of alternating parallel stripes with bright and dark contrast. Such stripes are almost aligned with the [100] edges of the substrate and they form domains of ~ 25 nm wide. As reported previously for Sr doped LMO films, they are typical of an ordered twin structure in rhombohedral films grown under tensile strain and they are the result of smooth strain accommodation during film growth.[36]

Static magnetic properties were measured using a Quantum Design SQUID magnetometer with the external magnetic field applied parallel to the substrate plane. Field-cooled temperature dependence of magnetization, Fig. 3(a), as well as isothermal hysteresis loops, Fig. 3(b), were measured. Note that magnetic measurements have been corrected using the diamagnetic contribution of the STO substrate. LMO films are strongly ferromagnetic and no significant differences were observed as a function of thickness for samples in the range of 10–25 nm, as evidenced in Fig. 3(a). Hysteresis loops recorded between 10 K and 200 K shown in Fig. 3(b) reflect the reduction of the saturation and remnant magnetization expected from the temperature dependence of magnetization presented in Fig. 3(a). On the other hand, coercive fields are very small (less than 15 mT at 100 K) and very similar for all the studied samples irrespective of their thickness, which suggests that in the thickness range analysed (10–20 nm) the microstructure of the samples is very similar. As mentioned above, although stoichiometric LaMnO₃ is an antiferromagnetic insulator, the presence of La vacancies leads to a mixed valence state of the Mn cation (Mn^{3+}–Mn^{4+}) that promotes the strong ferromagnetic interaction mediated by the standard double exchange mechanism. The obtained values of saturation magnetization $M(5$ K$) \sim 330$ emu cm^{-3} (corresponding to ~ 2.1 μ_B f.u.$^{-1}$) and transition temperature, $T_c \sim 290$ K, are slightly lower than expected for $La_{0.92}MnO_3$ composition. Two main mechanisms may be invoked to explain the reduction of the saturation magnetization in thin films with respect to the bulk value. First, it is known that at
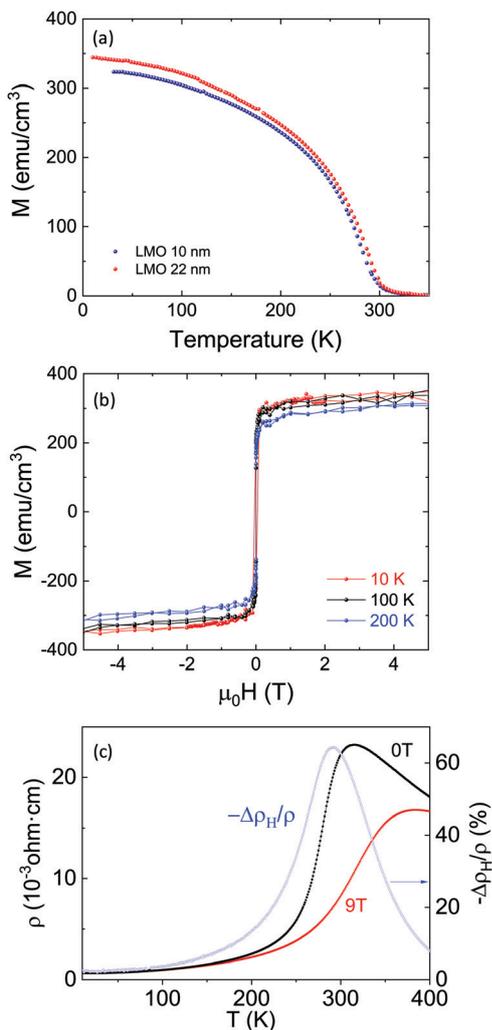
This journal is © The Royal Society of Chemistry 2019

J. Mater. Chem. C, 2019, **7**, 12633–12640 | **12635**

Fig. 3 (a) Temperature dependence of the magnetization measured at 5 kOe (field-cooled) for a 10 nm (blue symbols) and a 22 nm (red symbols) LMO film. (b) Hysteresis loops of a 10 nm LMO film measured at 10 K (red), 100 K (black) and 200 K (blue). (c) Temperature dependence of the electrical resistivity in the absence of an external magnetic field (0 T) (black curves) and with a magnetic field of 9 T (red curves). Magneto-resistance defined as $\Delta\rho_H/\rho = (\rho_H - \rho_0)/\rho_0$ is also shown (blue curves).

the interface with the substrate, a non magnetic dead layer may be formed due to the relaxation of biaxial stress during growth.[35] In this case, the measured magnetization values are affected by a wrong estimation of the real magnetic thickness. However, this dead layer tends to be of the order of a few unit cells and it cannot explain the strong deviation from the expected magnetization value in our films.[35] A second possibility is linked to the oxygen content of the film. In mixed valence manganites, where ferromagnetism is mediated by double-exchange interactions, saturation magnetization is controlled by the ratio Mn^{3+}/Mn^{4+}. A significant amount of oxygen vacancies implies a lower concentration of Mn^{4+} cations and thus a reduction of magnetization. This is the usual scenario in oxygen-deficient films. However, in $LaMnO_3$, a reduction of magnetization was also observed in overoxidized bulk samples.[28] Here, growth under strong oxidizing conditions promotes the

creation of cation vacancies (as interstitial sites are not available for excess oxygen) and Mn^{4+}-rich clusters may be formed. These clusters enhance antiferromagnetic correlations between Mn^{4+} cations and thus, full ferromagnetism is not achieved. So, we cannot disregard either of these mechanisms to explain our results shown in Fig. 3(a). In the standard double exchange picture, a metal–insulator transition (MIT) takes place, concomitant to the magnetic transition. We have measured the transport properties of the films, i.e., temperature dependence of their electrical resistivity and magnetoresistance, defined as $\Delta\rho_H/\rho = (\rho_H - \rho_0)/\rho_0$ by using a standard 4-probe van der Pauw configuration. The results are plotted in Fig. 3(c). Films exhibited a well defined metal-to-insulator transition with $T_{MI} = 280$ K defined as the inflexion point in the $\rho(T)$ curve. Residual resistance was found to be $\rho_{10K} = 6 \times 10^{-4}$ Ω cm. This value is lower than that reported for La-deficient LMO films grown by using physical methods.[29] At an applied magnetic field of 9 T, the maximum value of magnetoresistance was found to be 60% at 280 K, i.e., close to the transition temperature. As a summary, static magnetic and magnetotransport measurements confirmed that LMO films grown by the PAD route exhibit low disorder and strong ferromagnetic character driven by a double-exchange mechanism.

3 Magnetodynamic properties and discussion

The dynamic magnetic properties of LMO thin films as a function of temperature were studied by using a ferromagnetic resonance spectrometer (FMR) made of a broadband coplanar waveguide (NanOsc), inserted in a Physical Properties Measurements System (PPMS by Quantum Design). Measurements were performed at constant temperature using a sweeping external field at several fixed microwave frequencies (between 2 GHz and 17 GHz). Two main in-plane orientations were studied, either with the field applied along the main substrate edges, i.e., $\mu_0 H \parallel [100]STO$, or at 45° of the edges, i.e., $\mu_0 H \parallel [110]STO$. Fig. 4(a) shows typical FMR spectra obtained at 9 GHz and 100 K for both orientations. Note that, for a better comparison, measured signals (proportional to the first derivative of the microwave absorption intensity) have been renormalized to their respective maximum values. Each FMR spectrum may be fitted to the derivative of the sum of symmetric and antisymmetric Lorentzian components as previously suggested.[37] Solid lines in Fig. 4(a) correspond to the respective fitting curves. From these fittings, accurate values of the resonant field, H_{res}, and of the half-width at half-maximum linewidth, ΔH, are obtained. In transition metal oxide thin films, the presence of a small secondary resonant mode attributed to the presence of sample inhomogeneity is usually reported (secondary phase or regions with slightly different Curie temperature or magnetization that resonate at a different frequency/field).[38] In our case, in the whole studied temperature range, no signature of another resonant mode was observed.

The noticeable difference of the resonance field for both configurations just reflects a different saturation magnetization
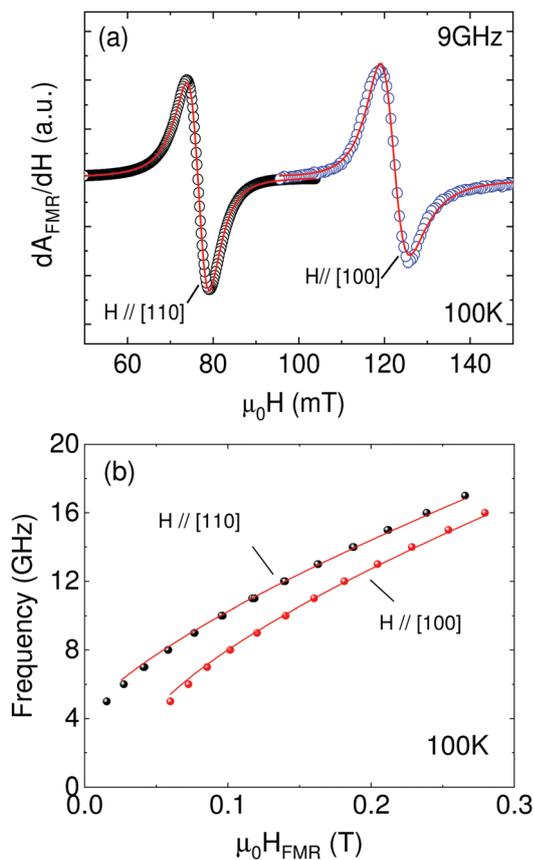
12636 | J. Mater. Chem. C, 2019, **7**, 12633–12640

This journal is © The Royal Society of Chemistry 2019

Fig. 4 (a) Ferromagnetic resonance spectra as a function of applied field for the two main in-plane orientations, i.e., [110] and [100], taken at 100 K and 9 GHz. Solid lines represent the best fittings to the sum of symmetric and antisymmetric Lorentz line shapes as explained in the main text. (b) Frequency dependence of the resonant field at 100 K for the two main in-plane orientations. Solid lines correspond to the best simultaneous fit of both experimental data to eqn (2) and (3) in the main text.

in each direction, i.e., in-plane magnetocrystalline anisotropy. In this case, [110] represents the in-plane easy axis (lower resonant field). Such in-plane anisotropy has been previously reported in other manganite based thin films[39] and it is believed to be a direct consequence of the highly epitaxial growth of materials with lower symmetry (orthorhombic/rhombo-hedral) onto cubic substrates as [110] is the in-plane projection of the [111] direction that, in manganite based perovskites, is the bulk easy axis.[40] It is worth noting that in the present case, no measurable differences in the FMR response between [100] and [010] directions have been observed. This is in agreement with previous results in thin films grown by chemical methods.[19] The absence of any extra in-plane uniaxial anisotropy, which, on the contrary, is usually observed in thin films grown by physical methods,[41] has been attributed to the different relaxation mechanisms involved during epitaxial growth using diverse techniques. This leads to different octahedral rotation patterns in the films to accommodate the stress and, as a consequence, to change orbital overlap and the magnetocrystalline anisotropy.

In the presence of in-plane anisotropy, the frequency dependence of the resonant field is no longer described by the simple

Kittel relationship and symmetry considerations need to be taken into account. For epitaxial thin films, a good approach is to consider a tetragonal symmetry, i.e., by assuming [100] and [010] directions to be equivalent. In this case, the resonance condition may be written as[41]

$$f = \frac{\gamma}{2\pi}\mu_0\left(H_R + H_{4ip}\cos 4\phi\right)^{1/2} \times \left[H_R + M_{eff} + \frac{1}{4}H_{4ip}(3 + \cos 4\phi)\right]^{1/2}$$

$$(1)$$

where γ is the gyromagnetic ratio, ϕ is the angle between the in-plane applied magnetic field and the [100] direction, and M_{eff} is defined as $4\pi M_{eff} = 4\pi M_S - 2K_\perp/M_S$ and includes the out-of-plane uniaxial anisotropy term $K_\perp$, whereas H_{4ip} is a four-fold in-plane anisotropy field, $H_{4ip} = + 2K_{4ip}/M_S$.

For the main in-plane directions, eqn (1) easily simplifies and it may be written for $H\|[100]$, $\phi = 0°$, as

$$f = \frac{\gamma}{2\pi}\mu_0\left(H_R + H_{4ip}\right)^{1/2}\left(H_R + M_{eff} + H_{4ip}\right)^{1/2}$$

$$(2)$$

and, for $H\|[110]$, $\phi = 45°$ as

$$f = \frac{\gamma}{2\pi}\mu_0\left(H_R - H_{4ip}\right)^{1/2}\left(H_R + M_{eff} + \frac{1}{2}H_{4ip}\right)^{1/2}$$

$$(3)$$

We have found that our experimental results may be nicely fitted by eqn (2) and (3). Fig. 4(b) shows an example for data taken at $T = 100$ K with solid lines being the best data fits according to the above equations.

Although eqn (2) and (3) are overparametrized, simultaneous and self-consistent fitting for both orientations allows obtaining reliable values of H_{4ip}. Its relation with temperature is plotted in Fig. 5(a). In this plot, error bars arise by averaging the data from several samples and taking into account the uncertainty in the fitting. First, we may see that H_{4ip} is negative, reflecting that indeed [110] is the in-plane easy axis. Secondly, it monotonously decreases when approaching the transition temperature. At 10 K, H_{4ip} is of the order of −100 mT. By using M_S values obtained from static SQUID measurements, this H_{4ip} value leads to an anisotropic constant of $K_{4ip}(10\ K) = -1.8 \times 10^4$ erg cm^{-3}, which is similar to the reported values for manganite-based thin films.[19,39,42,43] Anisotropic fields are expected to decay with temperature faster than saturation magnetization. In general, a power law dependence of the type $K(T)/K(T_0) = [M_S(T)/M_S(T_0)]^l$ is expected, where $K(T_0)$ and $M_S(T_0)$ are, respectively, the aniso-tropic field and magnetization at low temperature while l depends on the order of the anisotropy constant.[41] The inset in Fig. 5(a) shows the experimental dependence of $K_{4ip}(T)/K_{4ip}(T_0)$ as a function of $M_S(T)/M_S(T_0)$ with $T_0 = 10$ K. Experi-mental data are properly described by a power-law behavior that can be fitted by an exponent $l = 6$ (solid line).

On the other hand, γ and M_{eff} are closely interdependent during the fitting process and a wide interval of values leads to equally good fittings. Nevertheless, best fits have been obtained for $\gamma/2\pi = g\mu_B/h \sim 29.5$ GHz T^{-1} implying that the gyromagnetic factor, $g \sim 2.1$, is slightly higher than the spin-only value of 2 usually observed in manganites and it seems to suggest a small contribution from orbital angular momentum. With the
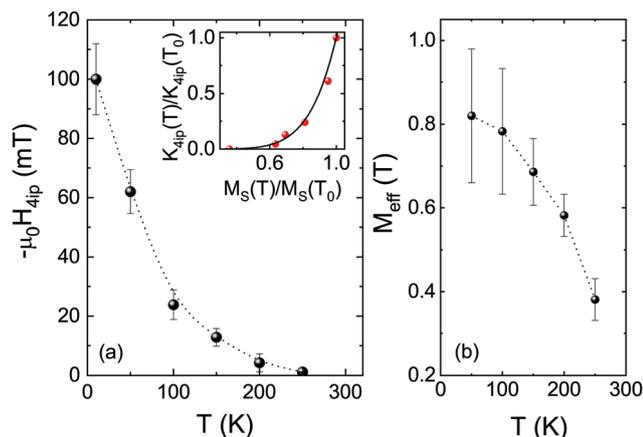
This journal is © The Royal Society of Chemistry 2019

J. Mater. Chem. C, 2019, 7, 12633–12640 | 12637

Fig. 5 (a) Temperature dependence of the fourfold in-plane anisotropy field, H_{4ip}, extracted from fits as shown in Fig. 4. The inset shows the power-law dependence of the normalized in-plane anisotropy constant $K_{4ip}(T)/K_{4ip}(T_0)$ as a function of normalized magnetization $M_S(T)/M_S(T_0)$. (b) Temperature dependence of M_{eff}. Error bars correspond to the uncertainty in the fit procedure and average over different samples. Dotted lines are guides for the eyes.

Table 1 Dynamic magnetic properties obtained from FMR and SQUID measurements

Parameter	LMO/STO
Gyromagnetic ratio, $\gamma/2\pi$	29.5 GHz T^{-1}
Gilbert damping, α at 150 K	1×10^{-2}
Inhomogeneous line-width, ΔH_0 at 150 K	<1 mT
In-plane anisotropic constant, K_{4ip} at 10 K	-1.8×10^4 erg cm^{-3}
In-plane anisotropy field, H_{4ip} at 10 K	-100 mT
Spin-mixing conductance, $g_{\uparrow\downarrow}$ at 150 K	$\sim 2 \times 10^{14}$ cm^{-2}

above assumptions, the temperature dependence of M_{eff} was obtained and it is plotted in Fig. 5(b) where error bars reflect uncertainty in the fitting parameters. By using the M_S values obtained from SQUID measurements, it easily follows that only negative values of $K_\perp$ are able to fit the experimental data. As mentioned above, $K_\perp$ includes not only any uniaxial magneto-crystalline anisotropy but also shape anisotropy and both are indistinguishable. A summary of the main magnetic parameters extracted from static and dynamic magnetic measurements is presented in Table 1.

The broadening of the resonance line, characterized by the linewidth ΔH, is a direct measure of the magnetic damping of the system. Damping is a key parameter for spintronic applications since it is closely related to the magnetization switching speed. Ideally, only intrinsic mechanisms contribute to the magnetic damping and, in such cases, the broadening of the ferromagnetic resonance linewidth may be described by a linear dependence on the frequency:[41]

$$\Delta H = \Delta H_0 + \frac{4\pi}{\gamma}\alpha f \tag{4}$$

In this expression, ΔH_0 represents an inhomogenous broadening and α is the intrinsic Gilbert damping. Fig. 6 shows the dependence of ΔH as a function of frequency obtained at
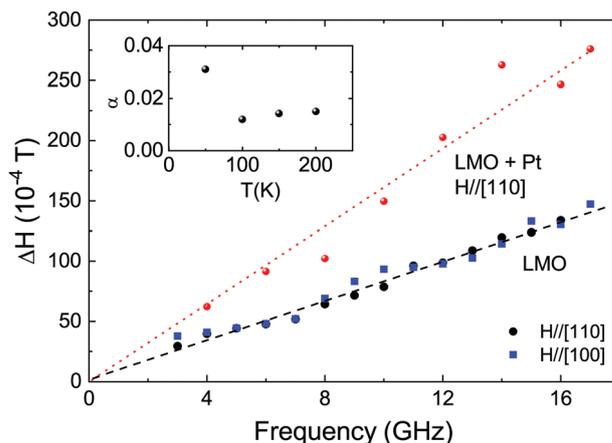

Fig. 6 Linewidth of ferromagnetic resonance of a LMO thin film as a function of frequency for two in-plane orientations taken at 150 K (blue squares and black dots). Linear behaviour corresponding to pure Gilbert damping may be observed and it is represented by the dotted line. The enhancement of damping after deposition of Pt as a cap layer is also presented (red points) and it may be associated with spin pumping through the FM/NM interface. Inset: Measured temperature dependence of Gilbert damping for the same LMO film.

150 K for the two in-plane directions, $H\|[100]$ and $H\|[110]$. Noticeably, linewidth broadening is independent of in-plane anisotropy and it is clear that the same straight line can nicely fit both curves. Two crucial results emerge from this result. First, ΔH_0, which accounts for extrinsic broadening arising from small magnetic inhomogenities in the sample, is very small ($\Delta H_0 \sim 1$ mT), confirming overall the high quality of thin films prepared by PAD. Secondly, the absence of anisotropy in ΔH and its linear frequency dependence exclude the presence of any noticeable two-magnon scattering contribution to damping, that is known to be a limiting factor when obtaining low-damping ferromagnetic conducting materials.[6] Furthermore, two-magnon scattering is usually activated by rough interfaces and surfaces and thus, their absence is in agreement with the smooth surface topography shown in Fig. 2. We may now soundly associate the slope of linear fits in Fig. 6 to the intrinsic Gilbert damping and by using eqn (4), we have obtained $\alpha_{LMO} \sim 1 \times 10^{-2}$ at $T = 150$ K. This value is comparable with Gilbert damping values reported in the literature for other complex oxide thin films with similar thicknesses grown by using physical methods[7,39,44] but there is still some room for improvement.[5] In particular, improving the critical temperature of LMO thin films, either by optimizing oxygen stoichiometry or cation deficiency, may lead to enhanced damping parameters at room temperature. The inset in Fig. 6 shows the temperature evolution of the Gilbert coefficient. In general, Gilbert damping is related to the spin–orbit coupling linking the precessing magnetic moment to the lattice. The annihilation of magnons generates scattering of electron–hole pairs. Depending on if this occurs at the same band (intraband) or not (interband), damping decreases with increasing temperature (conductivity-like, intraband) or increases with temperature (resistivity-like, interband).[2,5] Our results suggest that there is a large range of temperatures where damping is essentially

12638 | J. Mater. Chem. C, 2019, 7, 12633–12640

This journal is © The Royal Society of Chemistry 2019

constant (100 K < T < 200 K) and it increases rapidly at low temperature (T < 50 K), following a conductivity-like temperature dependence, usually associated with intraband behaviour. It is worth noting that our experimental finding is in agreement with the scenario suggested for manganites, where damping is governed by the so-called breathing Fermi surface model (intraband).[5]

The low damping parameter obtained in these PAD-grown LMO thin films opens the possibility to use them as a spin current source, through a spin pumping mechanism. In this phenomenon, a pure spin current is generated in a resonant ferromagnetic (FM) system and pumped into an adjacent non-magnetic (NM) conductor. When the conductor itself exhibits efficient spin–orbit coupling, as in the case of Pt, the spin-pumping mechanism will enhance the intrinsic Gilbert damping of the FM due to the extra dissipation channel of angular momentum because of spin pumping.[45] However, the diffusion of the spin-current towards the non-magnetic layer strongly depends on the so-called effective spin-mixing conductance $g_{\uparrow\downarrow}$ that measures the transparency of the FM/NM interface to spin current and their ability to relax within the non-magnetic layer. In this case, the Gilbert damping may be written as[2,46]

$$\alpha_{LMO+Pt} = \alpha_{LMO} + \frac{g\mu_B}{4\pi M t_{LMO}} g_{\uparrow\downarrow} \tag{5}$$

where t_{LMO} is the thickness of the spin source film, i.e., the LMO thin film, and μ_B is the Bohr magneton. The increase in Gilbert damping $\Delta\alpha = \alpha_{LMO+Pt} - \alpha_{LMO}$ has already been demonstrated for different FM/NM combinations, including alloys or oxides (as YIG[47] or LSMO[10]) as a spin source, grown by using vacuum techniques, such as sputtering or laser-ablation. However, it is believed to be extremely sensitive to the interface quality.[2] Thus, it is important to demonstrate that ex situ thin films grown by using chemical methods are suitable for spin generation. Red data points in Fig. 6 correspond to the FMR linewidth at 150 K along an easy axis of the same LMO thin film but after being capped with a 10 nm thick Pt film. In spite of higher noise in the curve, the increase in the damping is evident, and Gilbert damping is increased up to $\alpha_{LMO+Pt} \sim 2.5 \times 10^{-2}$. A rough estimation of the mixing conductance may be obtained from eqn (5). By using the values determined above, we have obtained $g_{\uparrow\downarrow}(150\ K) \sim 2 \times 10^{14}\ cm^{-2}$, comparable to that reported for other oxide films,[9] suggesting that interface transparency to spin transport is not inhibited by chemical growth methods.

4 Conclusions

We have demonstrated that $La_{0.92}MnO_3$ epitaxial thin films grown by polymer-assisted-deposition exhibit low roughness surfaces and magnetic properties fulfilling the requirements to be used as spin source active layers in heterostructures aimed for spintronic devices. Static magnetic and transport measurements show that LMO films are conducting and ferromagnetic, as expected from a double exchange scenario. On the other hand, dynamic magnetic properties were studied via broadband ferromagnetic resonance spectroscopy and we demonstrated

the presence of an in-plane four-fold magnetic anisotropy with [110] as an easy in-plane axis. In conjunction with microstructural analysis, this magnetic anisotropy resulted from the strained epitaxial growth of a LMO rhombohedral phase into the under-lying cubic $SrTiO_3$ substrate. Magnetic damping exhibits mainly intrinsic Gilbert damping without appreciable contributions from extrinsic mechanisms. In the presence of a 10 nm Pt capping, we have observed a clear enhancement of magnetic damping that may be indicative of effective spin injection into the Pt layer by spin pumping from the LMO film. The effective mixing conductance estimated from the measurements reveals an interface between ex situ chemically grown LMO and Pt with reasonable transparency to spin transport to be suitable for applications in spintronic devices.

Conflicts of interest

There are no conflicts to declare.

Acknowledgements

Notes and references

1 N. Locatelli, V. Cros and J. Grollier, Nat. Mater., 2014, 13, 11–20.

2 S. Azzawi, A. T. Hindmarch and D. Atkinson, J. Phys. D: Appl. Phys., 2017, 50, 473001.

3 A. Hoffmann and S. D. Bader, Phys. Rev. Appl., 2015, 4, 1–18.

4 L. Soumah, N. Beaulieu, L. Qassym, C. Carrétéro, E. Jacquet, R. Lebourgeois, J. Ben Youssef, P. Bortolotti, V. Cros and A. Anane, Nat. Commun., 2018, 9, 3355.

5 Q. Qin, S. He, W. Song, P. Yang, Q. Wu, Y. P. Feng and J. Chen, Appl. Phys. Lett., 2017, 110, 112401.

6 M. A. Schoen, D. Thonig, M. L. Schneider, T. J. Silva, H. T. Nembach, O. Eriksson, O. Karis and J. M. Shaw, Nat. Phys., 2016, 12, 839–842.

This journal is © The Royal Society of Chemistry 2019

J. Mater. Chem. C, 2019, 7, 12633–12640 | 12639

7   G. Y. Luo, C. R. Chang and J. G. Lin, *J. Appl. Phys.*, 2014, **115**, 17C508.

8   G. Y. Luo, M. Belmeguenai, Y. Roussigné, C. R. Chang, J. G. Lin and S. M. Chérif, *AIP Adv.*, 2015, **5**, 097148.

9   H. K. Lee, I. Barsukov, A. G. Swartz, B. Kim, L. Yang, H. Y. Hwang and I. N. Krivorotov, *AIP Adv.*, 2016, **6**, 055212.

10 S. Emori, U. S. Alaan, M. T. Gray, V. Sluka, Y. Chen, A. D. Kent and Y. Suzuki, *Phys. Rev. B*, 2016, **94**, 224423.

11 D. G. Schlom, *APL Mater.*, 2015, **3**, 1–6.

12 I. Safi, *Surf. Coat. Technol.*, 2000, **127**, 203–218.

13 M. Opel, *J. Phys. D: Appl. Phys.*, 2012, **45**, 033001.

14 M. A. A. Mamun, A. Haque, A. Pelton, B. Paul and K. Ghosh, *IEEE Trans. Magn.*, 2018, **54**, 1–8.

15 A. Haque, A. R. Mahbub, M. Abdullah-Al Mamun, M. Reaz and K. Ghosh, *Appl. Phys. A: Mater. Sci. Process.*, 2019, **125**, 1–9.

16 Q. X. Jia, T. M. McCleskey, A. K. Burrell, Y. Lin, G. E. Collis, H. Wang, A. D. Li and S. R. Foltyn, *Nat. Mater.*, 2004, **3**, 529–532.

17 J. M. Vila-Fungueiriño, B. Rivas-Murias, J. Rubio-Zuazo, A. Carretero-Genevrier, M. Lazzari and F. Rivadulla, *J. Mater. Chem. C*, 2018, **6**, 3834–3844.

18 H. Wang, J. Gazquez, C. Frontera, M. F. Chisholm, A. Pomar, B. Martínez and N. Mestres, *NPG Asia Mater.*, 2019, **11**, 41.

19 J. M. Vila-Fungueiriño, C. T. Bui, B. Rivas-Murias, E. Winkler, J. Milano, J. Santiso and F. Rivadulla, *J. Phys. D: Appl. Phys.*, 2016, **49**, 315001.

20 J. Suntivich, H. A. Gasteiger, N. Yabuuchi, H. Nakanishi, J. B. Goodenough and Y. Shao-Horn, *Nat. Chem.*, 2011, **3**, 546–550.

21 J. T. Mefford, W. G. Hardin, S. Dai, K. P. Johnston and K. J. Stevenson, *Nat. Mater.*, 2014, **13**, 726–732.

22 J. Garcia-Barriocanal, J. C. Cezar, F. Y. Bruno, P. Thakur, N. B. Brookes, C. Utfeld, A. Rivera-Calzada, S. R. Giblin, J. W. Taylor, J. A. Duffy, S. B. Dugdale, T. Nakamura, K. Kodama, C. Leon, S. Okamoto and J. Santamaria, *Nat. Commun.*, 2010, **1**, 82.

23 M. Gibert, P. Zubko, R. Scherwitzl, J. Íñiguez and J. M. Triscone, *Nat. Mater.*, 2012, **11**, 195–198.

24 X. R. Wang, C. J. Li, W. M. Lü, T. R. Paudel, D. P. Leusink, M. Hoek, N. Poccia, A. Vailionis, T. Venkatesan, J. M. Coey, E. Y. Tsymbal, Ariando and H. Hilgenkamp, *Science*, 2015, **349**, 716–719.

25 J. Roqueta, A. Pomar, L. Balcells, C. Frontera, S. Valencia, R. Abrudan, B. Bozzo, Z. Konstantinović, J. Santiso and B. Martínez, *Cryst. Growth Des.*, 2015, **15**, 5332–5337.

26 Y. S. Hou, H. J. Xiang and X. G. Gong, *Phys. Rev. B: Condens. Matter Mater. Phys.*, 2014, **89**, 64415.

27 A. Gupta, T. R. McGuire, P. R. Duncombe, M. Rupp, J. Z. Sun, W. J. Gallagher and G. Xiao, *Appl. Phys. Lett.*, 1995, **67**, 3494.

28 J. Töpfer and J. B. Goodenough, *J. Solid State Chem.*, 1997, **130**, 117–128.

29 I. Marozau, P. T. Das, M. Döbeli, J. G. Storey, M. A. Uribe-Laverde, S. Das, C. Wang, M. Rössle and C. Bernhard, *Phys. Rev. B: Condens. Matter Mater. Phys.*, 2014, **89**, 174422.

30 Y. K. Liu, H. F. Wong, K. K. Lam, C. L. Mak and C. W. Leung, *J. Magn. Magn. Mater.*, 2019, **481**, 85–92.

31 A. M. Zhang, S. L. Cheng, J. G. Lin and X. S. Wu, *J. Appl. Phys.*, 2015, **117**, 1–5.

32 A. Biswas, C.-H. Yang, R. Ramesh and Y. H. Jeong, *Prog. Surf. Sci.*, 2017, **92**, 117–141.

33 N. Sakai, H. Fjellvag and B. Lebech, *Acta Chem. Scand.*, 1997, **51**, 904–909.

34 D. Fuchs, L. Dieterle, E. Arac, R. Eder, P. Adelmann, V. Eyert, T. Kopp, R. Schneider, D. Gerthsen and H. V. Löhneysen, *Phys. Rev. B: Condens. Matter Mater. Phys.*, 2009, **79**, 1–9.

35 F. Sandiumenge, J. Santiso, L. Balcells, Z. Konstantinovic, J. Roqueta, A. Pomar, J. P. Espinós and B. Martínez, *Phys. Rev. Lett.*, 2013, **110**, 107206.

36 J. Santiso, J. Roqueta, N. Bagués, C. Frontera, Z. Konstantinovic, Q. Lu, B. Yildiz, B. Martínez, A. Pomar, L. Balcells and F. Sandiumenge, *ACS Appl. Mater. Interfaces*, 2016, **8**, 16823–16832.

37 M. Haidar, M. Ranjbar, M. Balinsky, R. K. Dumas, S. Khartsev and J. Åkerman, *J. Appl. Phys.*, 2015, **117**, 17D119.

38 S. Mercone, M. Belmeguenai, S. Malo, F. Ott, F. Cayrel, M. Golosovsky, B. Leridon, C. Adamo and P. Monod, *J. Phys. D: Appl. Phys.*, 2017, **50**, 045001.

39 Å. Monsen, J. E. Boschker, F. Macià, J. W. Wells, P. Nordblad, A. D. Kent, R. Mathieu, T. Tybell and E. Wahlström, *J. Magn. Magn. Mater.*, 2014, **369**, 197–204.

40 M. Konoto, T. Kohashi, K. Koike, T. Arima, Y. Kaneko, Y. Tomioka and Y. Tokura, *Appl. Phys. Lett.*, 2004, **84**, 2361–2363.

41 M. Farle, *Rep. Prog. Phys.*, 1998, **61**, 755–826.

42 M. Belmeguenai, F. Zighem, T. Chauveau, D. Faurie, Y. Roussigné, S. M. Chérif, P. Moch, K. Westerholt and P. Monod, *J. Appl. Phys.*, 2010, **108**, 063926.

43 F. Mompean, Z. Sefrioui, N. Reyren, T. Feher, M. Varela, C. Leon, J. Santamaria, M. Cabero, K. Nagy, F. Gallego, A. Sander and M. Rio, *APL Mater.*, 2017, **5**, 096104.

44 M. A. A. Mamun, A. Haque, A. Pelton, B. Paul and K. Ghosh, *J. Magn. Magn. Mater.*, 2019, **478**, 132–139.

45 Y. Tserkovnyak, A. Brataas and G. E. W. Bauer, *Phys. Rev. Lett.*, 2002, **88**, 117601.

46 Y. Liu, Z. Yuan, R. Wesselink, A. A. Starikov and P. J. Kelly, *Phys. Rev. Lett.*, 2014, **113**, 207202.

47 Y. Sun, H. Chang, M. Kabatek, Y.-Y. Song, Z. Wang, M. Jantz, W. Schneider, M. Wu, E. Montoya, B. Kardasz, B. Heinrich, S. G. E. te Velthuis, H. Schultheiss and A. Hoffmann, *Phys. Rev. Lett.*, 2013, **111**, 106601.

12640 | *J. Mater. Chem. C*, 2019, **7**, 12633–12640

This journal is © The Royal Society of Chemistry 2019